

Chapter 12

Global Wind Oscillation

Vittorio A. Gensini¹, Klaus M. Weickmann² and Caitlin Roufa¹

¹Department of Earth, Atmosphere and Environment, Northern Illinois University, DeKalb, IL, United States, ²Retired, Boulder, CO, United States

12.1 Introduction

This chapter, positioned as the 12th in a series of weather and climate oscillation overviews, is dedicated to a meticulous examination of the Global Wind Oscillation (GWO) and its derivation from Earth's atmospheric angular momentum (AAM). It aims to traverse the framework, foundational concepts, and broader implications of such an oscillation in the realm of planetary-scale atmospheric dynamics.

The GWO is a unique atmospheric oscillation when compared to the other well-documented oscillations such as the Madden–Julian Oscillation (MJO) or El Niño–southern Oscillation (ENSO). The latter oscillations aim to classify specific states of physical forcing mechanisms (e.g., latent heat release via anomalous tropical convection in the case of the MJO) measured in specific geographies. The GWO is an intriguing concept within the domain of weather/climate oscillations because it represents a global, comprehensive framework that captures the essence of global atmospheric variability. The idea of a global oscillation in kinematic properties (e.g., wind, momentum) impacting weather, climate, and the Earth's rotational dynamics, prompts a detailed exploration of its constituents, implications, and future research avenues herein.

The subsequent sections are structured to provide an in-depth analysis of the GWO, emphasizing its components, intricacies, and patterns. This exploration, while comprehensive, demands a conscientious approach that examines a variety of physical processes across a range of spatiotemporal scales.

12.2 Fundamentals

The GWO can be succinctly defined as the periodic and quasiperiodic variations in Earth's global wind patterns. These oscillations are not merely random fluctuations; they represent systematic shifts in atmospheric dynamics influenced by a handful of physical processes. At its core, the GWO encapsulates the Earth's synoptic and planetary-scale atmospheric variability, manifested in alterations in kinematic properties such as wind speed, direction, and momentum. At the heart of understanding the GWO lies the concept of AAM.

AAM quantifies the rotational dynamics of the atmosphere, encompassing Earth's synoptic and planetary-scale atmospheric variability. AAM has been a key topic of research since the 1950s and has origins dating back to Bernoulli and Hadley in the 1700s. Starr,¹ Starr and White,² and Lorenz³ were among the first to describe and calculate fundamental aspects of the AAM budget. Interested readers can find the historical evolution of this knowledge documented in Oort⁴ and Rosen,⁵ with a more recent overview found in Egger et al.⁶ The concept of AAM serves as an effective lens through which the influence of factors like mountains, wind stresses on the surface, and various transport processes can be analyzed over periods ranging from intraseasonal to interdecadal. AAM stands out as a significant indicator of extensive zonal flows due to its relationship with length-of-day measurements and other oscillations discussed in this book.^{7–19}

Given the importance of AAM, let's first examine the concept of angular momentum and its application to Earth's atmosphere.

12.2.1 Angular momentum

Angular momentum (M) is a fundamental vector quantity of any rotating system that aims to measure rotational momentum. It can be mathematically written as the cross product between a vector with position and distance r from an origin about which the body rotates and the linear momentum (i.e., a product of mass m and velocity v):

$$M = r \times mv \quad (12.1)$$

Earth's angular momentum budget represents a beautiful example of how the atmosphere, oceans and solid Earth interact as individual components. Each of these components is directly linked to the conservation of Earth's angular momentum, as angular momentum is a conserved quantity in any closed system—a derivation that is beyond the scope of this chapter but can be found in the aforementioned reviews.

The total angular momentum of the atmosphere, oceans, and Earth's surface does not change except for a slow secular decrease due to the gravitational force exerted by planets.⁴ However, there is a transfer of momentum between these three components, consisting of a budget that is conserved. Thus if angular momentum increases in the atmosphere, it must have been transferred from one of the other components into the atmosphere. Analogously, if the atmosphere loses angular momentum, it needs to be transferred to one of the other components. Evidence of this transfer can be seen in changes in the length of day (LOD) resulting from the exchange of angular momentum between the solid Earth and the atmosphere.^{5,20–25}

12.2.2 Atmospheric angular momentum

Earth's AAM, M_E , can be divided into two distinct components: the total rotational atmospheric mass component, denoted as M_Ω , and the relative atmospheric component, M_R :

$$M_E = M_\Omega + M_R \quad (12.2)$$

The mass component represents the angular momentum that the atmosphere would possess if it were entirely stationary, both vertically and horizontally, in relation to the ground. In contrast, the relative component of AAM arises from the atmospheric motion compared to Earth's rotation. The units of M_E are N · m · s (or SI base of kg · m²/s). Primarily, variations in M_Ω stem from fluctuations in the atmospheric mass and pressure within a specific atmospheric region, whereas changes in the relative component arise from the vertical and horizontal distribution of wind. M_Ω has several aliases in formal research manuscripts (e.g., the Ω momentum term, the pressure term, the matter term, Earth angular momentum term) and M_R is sometimes referenced as the motion or wind term.⁶

To calculate M_Ω , one must know the volumetric (zonal, meridional, and vertical) integral of Earth's atmospheric mass (i.e., density). Since atmospheric density at any given level is challenging to quantitatively measure, surface pressure and gravity are typically substituted,²⁶ thus:

$$M_\Omega = \frac{a^4 \Omega}{g} \int_{\lambda=0}^{2\pi} \int_{\phi=-\frac{\pi}{2}}^{\frac{\pi}{2}} p_{\text{sfc}} \cos^3 \phi d\phi d\lambda \quad (12.3)$$

where a is Earth's radius (m), Ω is Earth's angular velocity (rad/s), g is Earth's gravity (m/s²), and p_{sfc} is pressure (Pa) at Earth's surface. To provide a sense of scale, we calculate the mean value of M_Ω from 1970 to 2021 from the NCEP/NCAR reanalysis²⁷ to be 1.02×10^{28} N · m · s. As one would expect from the equation, M_Ω is maximized over the tropics and approaches zero near the poles (Fig. 12.1). M_Ω does exhibit annual variability (maximum in boreal fall and minimum in boreal spring), but it is orders of magnitude smaller, with a range of approximately 4.9×10^{24} N · m · s.

The relative component of AAM (M_R), while much smaller than M_Ω , is far more variable given its dependence on zonal wind speed. M_R can be thought of as the component of angular momentum due to the flow of air relative to Earth's rotational direction, specifically focusing on how the moving air (i.e., wind) in the atmosphere contributes to the Earth's overall angular momentum. A net westerly wind ($u > 0$) can increase the Earth's spin slightly due to alignment with Earth's rotational direction. Conversely, a net easterly wind against the Earth's rotation would decrease the spin slightly.²⁸ Calculation of M_R requires understanding of the 3-D distribution of zonal wind:

$$M_R = \frac{a^3}{g} \int_{\phi=-\frac{\pi}{2}}^{\frac{\pi}{2}} \int_{\lambda=0}^{2\pi} \int_p^{p_{\text{sfc}}} u \cos^2 \phi d\phi d\lambda dp \quad (12.4)$$

where a is Earth's radius (m), g is Earth's gravity (m/s²), and u is the zonal wind speed (m/s). M_R has a much larger dependence on the atmosphere's general circulation, and as mentioned, has a significantly greater range of intraseasonal

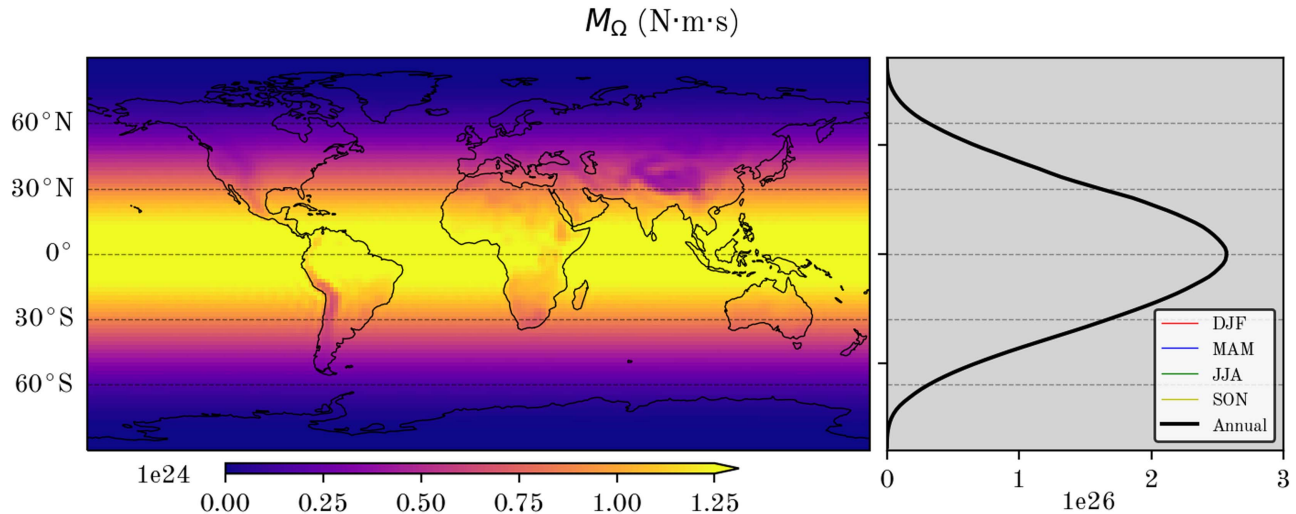


FIGURE 12.1 Earth's average rotational atmospheric mass component of AAM (M_Ω), as calculated by NCEP/NCAR reanalysis 6-hourly data on the native Gaussian T62 grid from 1970–2021. *Panel left* shows the global distribution, and *panel right* indicates the mean zonal profile by latitude band (roughly 1.9° at the equator). Map lines delineate study areas and do not necessarily depict accepted national boundaries.

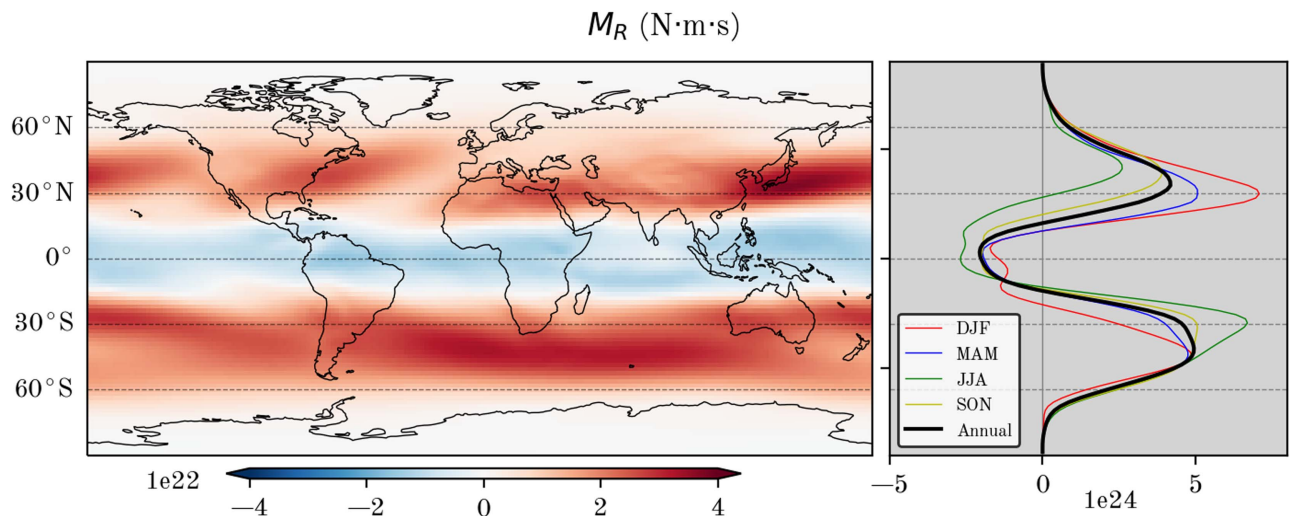


FIGURE 12.2 As in Fig. 12.1, except for the Earth-relative atmospheric component of AAM (M_R). Map lines delineate study areas and do not necessarily depict accepted national boundaries.

change relative to the long-term mean.²⁶ This makes it an interesting candidate when viewed through the lens of weather and climate variability.

Seasonal variation in M_R is evident, with a sharp minimum occurring in July–August (approximately 1.03×10^{26} N·m·s) and a broader maximum in November–May^{6,29,30} (approximately 1.5×10^{26} N·m·s). A climatological distribution of M_R is shown in Fig. 12.2. Seasonal differences in the minimum and maximum values of M_R result from topographic differences between the Northern and Southern Hemispheres. There is larger M_R variability in the Northern Hemisphere, where the proportion of land surface to ocean is greater than in the Southern Hemisphere.⁶ Differences in the Earth's surface topography affect the amount of momentum transferred between the solid Earth, oceans, and the atmosphere through surface stress and orographically induced pressure variations. The larger variability in the Northern Hemisphere drives stronger maxima in DJF than in JJA.^{30,31}

Intraseasonal variability of AAM, like seasonal variability, is due to fluctuations in M_R . High-frequency intraseasonal AAM flux is primarily due to surface pressure differences across topography (e.g., large mountain ranges) resulting from synoptic extratropical weather systems.³² As with the seasonal contribution, the midlatitudes of both hemispheres provide the dominant contribution to intraseasonal AAM variation. The MJO, the ENSO, and several other atmospheric

oscillations have a significant impact on both intraseasonal, seasonal, and annual AAM variation.^{6,9,16,18,33} These interactions are discussed in more depth in Section 12.3 of this chapter.

The transport of AAM (i.e., flux divergence) can be defined as the divergence of the flow rate of angular momentum ($\text{kg} \cdot \text{m}^2/\text{s}^2$) and is conceptualized as the Eulerian time averaged differential of angular momentum with respect to time. Three primary transports dominate the flux of relative AAM: large-scale eddies, surface stress, and pressure differences across orography.^{6,28} These transports drive AAM flux in both the horizontal and the vertical. Since M_Ω is constant through time due to conservation of mass between the solid Earth and atmosphere, the total AAM transport in the horizontal is solely due to changes in M_R . When considered in a zonal cross-section, the flux of AAM can be viewed as cells of momentum exchange between the Earth and atmosphere, and transport between the tropics and midlatitudes (c. f. Fig. 11.9 in Ref. 28).

AAM originates in the tropics as a result of momentum transfer between the solid Earth and oceans and the atmosphere due to surface friction. This is driven by the prevailing surface tropical easterlies flowing opposite the rotational direction of the Earth, with maximum flux centered around latitudes with maximum easterly wind velocity.^{6,34} At these source regions, AAM is transported vertically as part of the upward branch of the Hadley Cell circulation. Vertical transport of AAM is generally symmetric about the equator, with seasonal shifts in location related to the position of the ITCZ.

Thereafter, AAM is advected poleward via large-scale eddies in the upper branch of the Hadley Cell circulation in the upper troposphere. Both stationary and transient eddies are present in the advection of AAM, with transient eddies as the dominant mode of poleward transport. These eddies, along with the prevailing surface winds, drive a southwest-to-northeast (northwest-to-southeast) tilt in the streamlines of AAM transport in the Northern (Southern) Hemisphere, which can be seen in the climatological mean tilted pattern of flux divergence in Fig. 12.3. Poleward transport terminates in the midlatitudes where vertical transport occurs via eddies at the downward branches of the Hadley and Ferrel Cells. It is here that prevailing westerly surface winds drive pressure differences across mountain ranges, transporting AAM downward, out of the atmosphere and into the solid Earth and oceans. Note the effects of orographic pressure differences due to the major mountain ranges, particularly the Rocky Mountains, the Himalayas, and the Andes in Fig. 12.3, as well as the stronger relative flux divergence in the Northern Hemisphere.

Analyzing angular momentum budget transfers involves monitoring the first differential of the angular momentum equation with respect to time, which can be written as

$$\frac{dM_E}{dt} = r \times F \quad (12.5)$$

where F is equal to the product of mass (m) and acceleration (a), the latter of which appears after the differentiation of velocity (v) with respect to time. Thus, the time rate of change of angular momentum for a system is equal to the cross product of its distance from the origin about which it rotates and the total force applied. This cross product ($r \times F$) is referred to as torque.

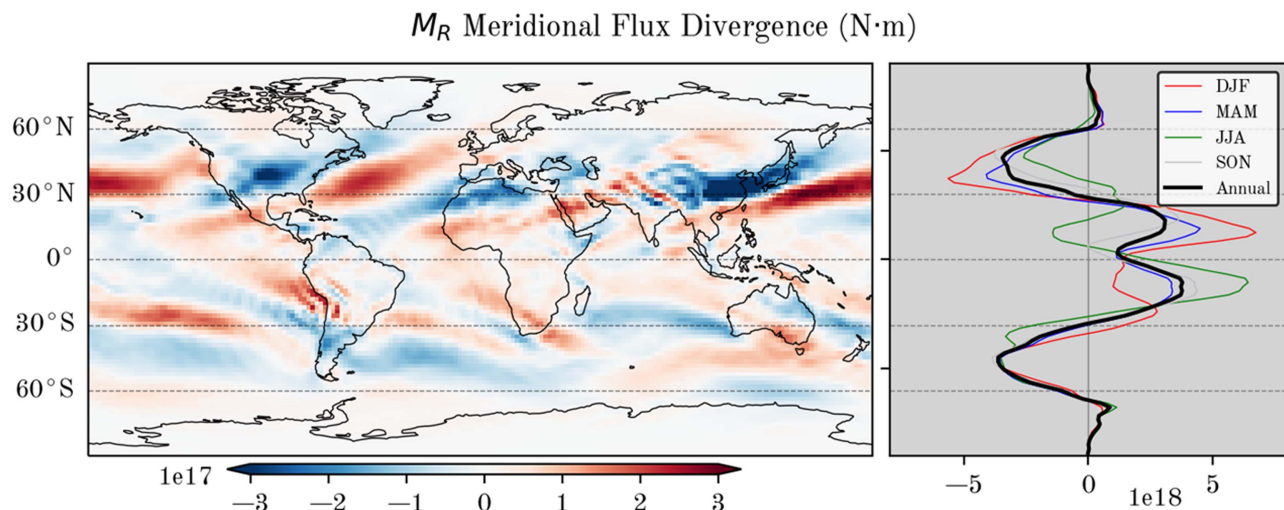


FIGURE 12.3 As in Fig. 12.1, except for the meridional flux divergence of relative AAM (M_R). Map lines delineate study areas and do not necessarily depict accepted national boundaries.

12.2.3 Torque

If a torque, or a “turning force,” is applied to a rotating object, it will slow down or speed up the object’s rate of rotation about the origin, or even change its direction of rotation. Through friction and spatial pressure differences, the atmosphere applies these rotational forces to the solid Earth which causes the rotation rate of the solid earth to either speed up or slow down, and in doing so, the atmosphere’s angular momentum decreases or increases as it imparts or receives angular momentum to or from the Earth.¹ In essence, torque is the mechanism that facilitates the transfer of angular momentum between the Earth’s various components: the atmosphere, oceans, and solid Earth. Herein, we describe a torque that increases AAM to be a positive torque and one that decreases AAM to be a negative torque.

Numerous torques can act to change AAM, including solar winds, electromagnetic forces, celestial torques from planets and Earth’s moon, moisture torque, and ocean/continent torque.^{6,16,28} However, scale analyses reveal that only friction and mountain torque play a significant role in altering the budget of AAM. In weather and climate studies, these torques are generally given in the unit Hadley, abbreviated Had, where 1 Had is equivalent to $10^{18} \text{ N} \cdot \text{m}$.

12.2.4 Friction torque

Friction torque is a product of the interaction between the free-moving atmosphere and the Earth’s surface. As winds traverse the surface, they encounter friction, especially in the planetary boundary layer where direct contact with the surface occurs. This frictional interaction reduces the velocity and associated momentum of the wind, generating a torque that affects Earth’s rotation. Friction torque not only impacts local wind patterns, especially in regions of significant surface roughness, but also plays a role in tidal interactions along coastlines. Factors such as the degree of surface roughness, wind speed, and wind direction influence the magnitude and direction of this torque. If there is a net global westerly surface wind (i.e., a net surface wind blowing from west to east), the atmosphere will speed up Earth’s rotation, transfer angular momentum to the Earth, and thus the atmosphere loses angular momentum. The inverse to this would be a net easterly surface wind, where the atmosphere slows down the rotation of the Earth and angular momentum is transferred from the Earth to the atmosphere. Thus, in the tropics, surface winds typically blow from east to west (i.e., trade-wind easterlies), resulting in a positive friction torque. In contrast, midlatitude surface flow often blows from west to east, leading to a negative observed friction torque.

Friction torque (T_F) is the global integral of the zonal surface friction stress per unit area (τ_f , units Pa) and can be written as

$$T_F = a^3 \int_{\lambda=0}^{2\pi} \int_{\phi=-\frac{\pi}{2}}^{\frac{\pi}{2}} \tau_f \cos^2 \phi d\phi d\lambda \quad (12.6)$$

where a is Earth’s radius, λ is longitude, and ϕ is latitude. The units of T_F are torque ($\text{N} \cdot \text{m}$); equivalent to $\text{kg} \cdot \text{m}^2/\text{s}^2$. A meridional cross-section of climatological zonal mean friction torque (Fig. 12.4) shows that the Southern Hemisphere midlatitudes are the largest source of negative friction torque, and on average, act to speed up the rotation rate of the Earth (therefore serving as an AAM sink). Seasonal peaks are noticed in the tropics during each hemisphere’s respective winter, and there is a clear signal of decreasing negative friction torque associated with a weakening net westerly zonal wind in the Northern Hemisphere midlatitudes during boreal summer.

12.2.5 Mountain torque

Mountain torque arises from the interaction of the atmosphere with the Earth’s topographical features, most notably large mountain ranges. As flows occur over these terrains, pressure differences develop between the windward and leeward sides of mountains. This disparity in pressure exerts a net force perpendicular to the mountain range, resulting in torque that can influence Earth’s rotation. Consider a mountain with relatively higher pressure on the west side versus lower pressure to the east. The atmosphere will exert an eastward-directed torque that causes the Earth to increase its rate of rotation, imparting angular momentum from the atmosphere to the solid Earth. This reduces AAM. The opposite case, where there is higher pressure on the east side of the mountain, will slow the Earth’s rotation down, reducing the solid Earth’s angular momentum, and imparting it to the atmosphere. Mountain torque (T_M) can be defined as

$$T_M = a^3 \int_{\lambda=0}^{2\pi} \int_{\phi=-\frac{\pi}{2}}^{\frac{\pi}{2}} h \frac{\partial p_{\text{sfc}}}{\partial x} \cos^2 \phi d\phi d\lambda \quad (12.7)$$

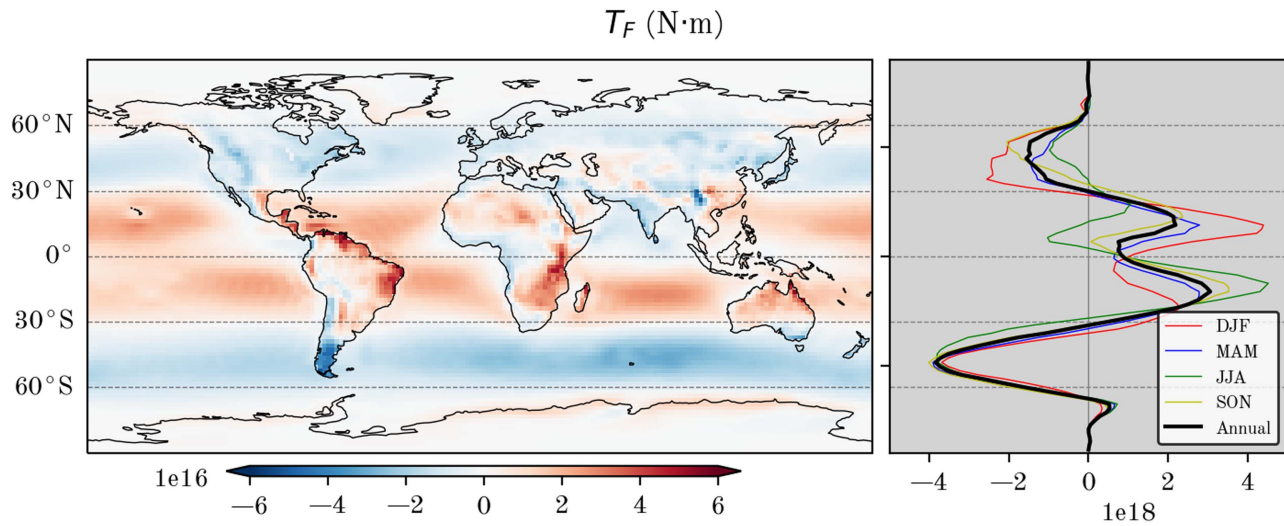


FIGURE 12.4 As in Fig. 12.1, except for friction torque (T_F). Map lines delineate study areas and do not necessarily depict accepted national boundaries.

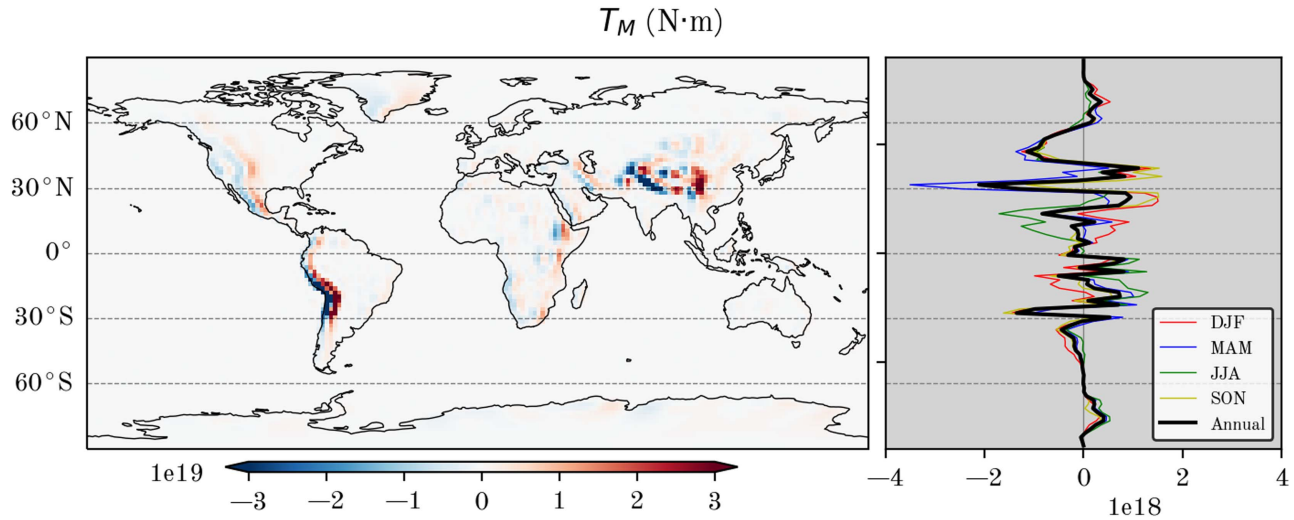


FIGURE 12.5 As in Fig. 12.1, except for mountain torque (T_M). Map lines delineate study areas and do not necessarily depict accepted national boundaries.

where a is Earth's radius, λ is longitude, ϕ is latitude, h is terrain height, p_{sc} is surface pressure, and x is the zonal direction. One should use caution in the calculation of T_M due to the sensitivity of the zonal differential of topography and surface pressure to the selected numerical scheme and grid representation.³⁵

From a climatological perspective, the Himalayas and Rocky Mountains exert the largest mountain torques, with the Andes also playing a modest role.^{26,32,36} AAM is typically lost, and the atmosphere decelerates, due to the pressure differences across these mountain ranges (preference for time-averaged leeward side low-pressure with an eastward-directed torque). Fig. 12.5 shows the spatial and zonal mean seasonal contributions of mountain torque.

12.2.6 Other torques

As previously mentioned, other sources of torque on the Earth system exist, but they are generally orders of magnitude smaller than friction and mountain torques. For brevity, only one additional torque will be mentioned here—associated with gravity wave drag—due to its prevalence in large-scale atmospheric models. In short, global numerical weather analysis and prediction systems (e.g., reanalyses) must also account for forces and torques that are unresolvable due to inadequate horizontal grid spacing. For example, a mountain range with very jagged terrain is not well represented in a general circulation model with a relatively coarse horizontal grid spacing of $1^\circ \times 1^\circ$. Flow over such topography,

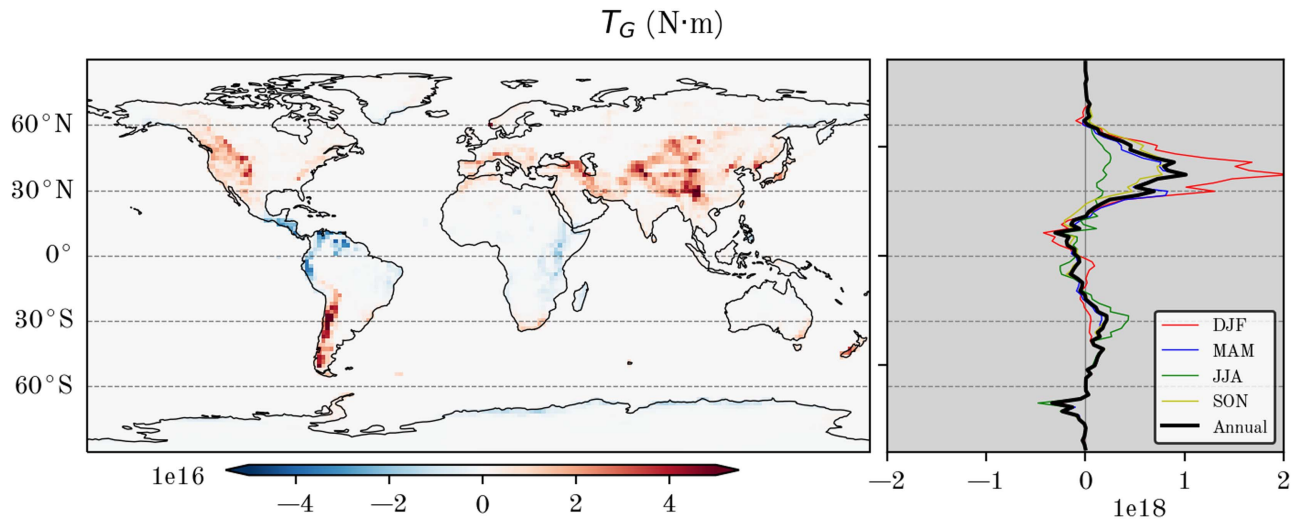


FIGURE 12.6 As in Fig. 12.1, except for zonal gravity wave drag torque (T_G). Map lines delineate study areas and do not necessarily depict accepted national boundaries.

as well as other highly dynamic atmospheric processes, can generate gravity waves that are subgrid scale. Gravity waves can play a significant role in altering atmospheric properties, and to account for this, a parametrization known as gravity wave drag is utilized.³⁷ Gravity wave drag (sometimes aliased as gravity wave stress per unit area; units Pa) torque can be computed by substituting the zonal component of gravity wave drag into the equation for friction torque in place of the zonal surface friction stress. As you might expect, the largest values of mean gravity wave drag are found in areas with varied orography (Fig. 12.6).

Eq. (12.5) establishes a relationship between the total time rate of change of AAM and the total torque. The sum of the torques, particularly friction, mountain, and gravity wave drag torques, yields the net torque, which must be equivalent to the time tendency of AAM according to the conservation of momentum. This relationship can be defined by

$$\frac{dM_E}{dt} = T_F + T_M + T_G \quad (12.8)$$

where T_F , T_M , and T_G are the friction, mountain, and gravity wave drag torques respectively.^{6,26,33} Again, a net positive torque will increase AAM through time, while a net negative torque will decrease AAM through time. AAM budget closures can help determine how well global climate models perform as well as their basis in physical reality. Ideally, both sides of this equation should be exactly equal for a closed momentum budget; however, nearly all global forecast and reanalysis systems show some biases between AAM and torque in addition to decadal trends.^{26,38–43} Some insight is provided by the contributions of the torques to the AAM budget through spectral analysis.

Spectral analysis has been useful in determining the contributions of torques to the AAM budget at different timescales and can be represented by power spectra diagrams.^{21,32} Power spectra of the AAM components (Fig. 12.7A) show that for high-frequency timescales (periods under approximately 15 days), both the M_R and M_Ω tendencies contribute equally to the AAM budget. At periods beyond approximately 15 days, M_R dominates budget transactions. Power spectra of the torques show timescale-dependent differences in contributions to the total torque and AAM budget (Fig. 12.7B). On periods of less than approximately 20 days, mountain torque dominates friction torque by an order of magnitude.^{26,32,44} This high-frequency dominance of the mountain torque is due to the motion of synoptic-scale weather systems across mountain ranges, as determined by several previous works.^{14,24,45,46} At periods longer than 30 days, the contributions of the mountain and friction torque are roughly equivalent to the global budget. When considering the zonal budget, however, the friction torque dominates at intraseasonal timescales.⁴⁴

The transports discussed in the prior section become apparent when the budget is viewed on an intraseasonal timescale. Going back to Fig. 12.3 (relative M_R flux divergence), one can infer the poleward propagation of relative M_R flux convergence associated with tropical convective anomalies.^{47,48} The poleward flux of relative M_R from the tropics also drives and leads the torques in the subtropics by approximately 10 days, where peak friction torque (and peak zonal mean surface wind) leads peak mountain torque by approximately 10 days. As poleward propagation continues toward the midlatitudes, M_R flux divergence drives and typically leads the torque by 1–3 days.⁴⁴ Further discussion of the lags and leads of torques with respect to the GWO are presented in the next section.

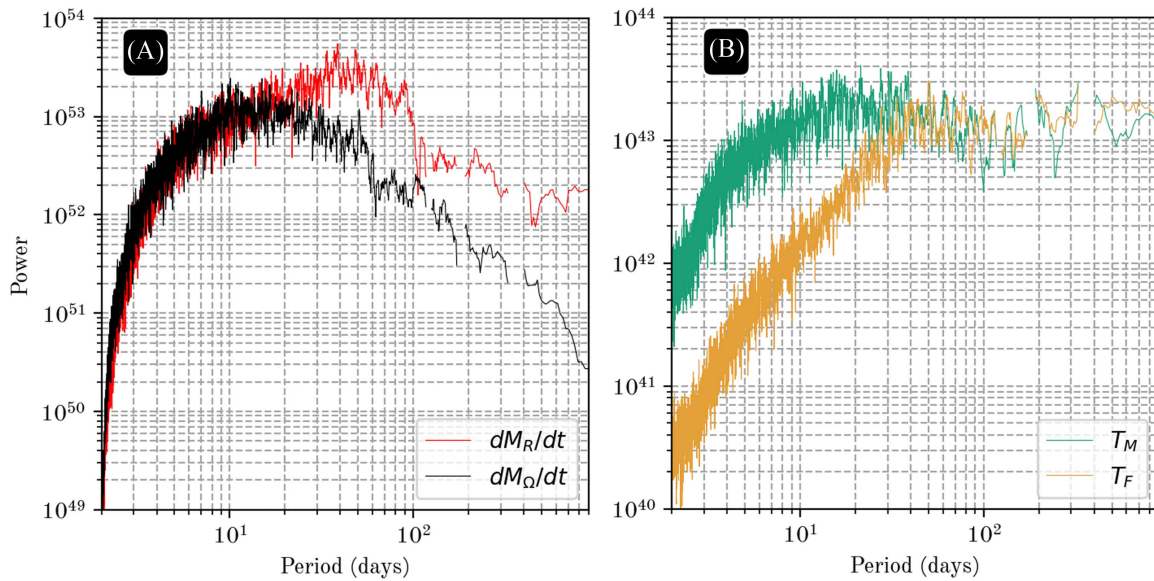


FIGURE 12.7 Power spectral density (with the first three seasonal harmonics removed) of (A) M_Ω tendency (black) and M_R tendency (red) as well as (B) T_M (green) and T_F (orange) based on NCEP/NCAR reanalysis 6-hourly data (1970–2021).

12.3 Defining the Global Wind Oscillation

We have discussed that *global* AAM can be changed through mountain torques produced by surface pressure differences across sloping east-west terrain, the frictional torque through changes in the distribution of subtropical trade winds versus midlatitude westerly surface flow, and gravity wave drag through vertically propagating gravity waves.⁶ Zonal AAM variations bring in other physical processes, like meridional AAM transports by eddy and time-mean flows as well as the Coriolis torque. The global torques' power spectra imply different “peaks” and/or red noise decay time scales. Dominant mountain torque forcing at <10 -day periods transitions to forcing by both friction and mountain torques for >10 -day periods. The total M_E tendency is dominated by M_R tendency (wind) for >20 -day periods while both pressure and wind contribute to <15 -day tendencies.

At its most fundamental level, the GWO is a red noise process where the friction torque leads the mountain torque and through meridional momentum transports, produces AAM anomalies in the upper subtropical-midlatitude atmosphere. Distinct synoptic patterns around major topography and in the subtropical-midlatitude jet stream have been used to make 1–3-week predictions using the GWO¹⁷ and to examine the intraseasonal variability of severe weather in the central United States.^{49,50}

12.3.1 The friction-mountain torque index cycle

Weickmann et al.³³ and Weickmann⁵¹ developed the idea of a friction-mountain torque index cycle for the GWO using cross-spectral analysis and linear regression with global integrals as independent variables. They created this index cycle based on zonal mean predictions from the mountain torque³³ (Fig. 12.5) and the frictional torque⁵¹ (Fig. 12.4). Cross-spectral analysis revealed that the friction torque leads the mountain torque during episodes of large AAM tendency. The key anomaly sequence for a negative $\frac{dM_R}{dt}$ is as follows:

1. Strong northward momentum transport across 35°N occurs in the upper atmosphere. Increased midlatitude westerlies reach the surface giving $TF < 0$ and when they flow over mountains contribute $T_M < 0$ causing M_R to decrease.
2. Subtropical easterly wind anomalies eventually also reach the surface and strengthen the tradewinds leading to $TF > 0$ and halting the rate of M_R decrease.
3. Negative M_R anomalies are further damped by the weakening $TF > 0$ although occasionally, a stochastic event triggers weakened flow over mountains, leading to $T_M > 0$ and an increase in M_R . This can give the appearance of a cycle.

The global 250 hPa streamfunction and surface pressure anomalies contributing to the global torques are illustrated in Weickmann et al.³³ and Weickmann⁵¹ and provide more detail on the evolution of circulation anomalies related to the index cycle.

The MJO and the GWO are different phenomena although both exhibit intraseasonal variability and can interact through large-scale circulation patterns forced separately by tropical convection and the global torques.¹⁷ The GWO emerged from the global synoptic dynamic model constructed by Weickmann and Berry,⁵² which combined four different time scales and their regional to global circulation patterns.

12.3.2 The Madden–Julian Oscillation

The MJO is summarized extensively in [Chapter 2](#). It has the closest time scale to the GWO and is most likely to be intertwined with it. Changes in global AAM during an MJO are driven primarily by friction torque,²⁶ which strengthens and then weakens as convection moves eastward from the Indian Ocean to the dateline. However, in individual cases, the mountain torque dominates so the relative contribution by the two torques is still in doubt. Further comparisons between the MJO and GWO AAM variations are presented next using two-dimensional phase spaces.

12.3.3 The Global Wind Oscillation and Madden–Julian Oscillation phase spaces

A convenient way to visually organize these modes for further analysis is the phase space diagram introduced for the MJO by Wheeler and Hendon based on the real-time multivariate MJO (RMM) index.⁵³ Weickmann and Berry¹⁷ introduced a similar construct involving global M_R and global $\frac{dM_R}{dt}$ to produce a 2-D GWO phase space. Instead of plotting RMM1 and RMM2 (for a MJO phase space diagram), the GWO phase diagram uses AAM1 (y-axis) and AAM2 (x-axis), where AAM1 represents the standardized anomaly of M_R and AAM2 represents the standardized anomaly of tendency ($\frac{dM_R}{dt}$). The GWO phase space can be used to measure M_R variations associated with ENSO, the MJO and IPO/PDO variability, but the fundamental GWO dynamics are stochastic with a approximately 10-day decay time scale.

[Fig. 12.8](#) shows the GWO and MJO phase spaces using annual data from 1979 to 2019. The curved lines with dots represent lag trajectories from day 0 to day +15 emanating from 16 phases with alternating magnitudes of >1.0 and >2.0 standard deviations (σ). The GWO trajectories ([Fig. 12.8A](#)) show a period of rapid growth of anomalies followed by persistence in phases 3 and 7, consistent with a stochastic process with a 10–15-day decay time scale. They have a “hooked” appearance as they cross maximum AAM (phase 6.5) or minimum AAM (phase 2.5) where the total torque is zero. Rather than eastward moving tropical convection as during an MJO, a sequence of global surface torques having the same sign is observed: the frictional torque leads the mountain torque, and both are preceded and followed by meridional AAM transports across 35° latitude that either initiate or amplify the signal. The dominant signals occur across the Asia–Pacific Ocean–Americas region and are the largest in the winter hemisphere. When these physical processes have the same sign, rapid growth to one of the persistent states shown by the lag composite trajectories can occur.

[Fig. 12.8B](#) shows the MJO phase space defined by the RMM index,⁵³ which represents the first two combined EOFs⁵⁵ of outgoing longwave radiation (OLR) and 250 and 850 hPa zonal wind. Annotations show the location of tropical convection during phases 1–8 and the evolution of eastward propagating zonal circulation cells during phases A–F as proposed by Madden and Julian.⁵⁴ The trajectories illustrate how different the two phenomena are. The MJO’s eastward propagation evident in the trajectories generally extends about 2–3 phases (approximately 10–15 days) into the future before weakening to a magnitude of $<1 \sigma$ anomaly. The seasonal trajectories during boreal winter show the most coherent eastward propagation and a stronger oscillatory nature.

The phases preferred during El Niño and La Niña events are marked on both phase spaces. They help emphasize that the phase numbers are not equivalent and cannot be compared directly. The GWO space needs to be rotated counterclockwise 1.5 phases for the ENSO states to line up. This is a consequence of how the different spaces were defined. The 3-D phase space discussed later provides a physical link between the GWO torques and the MJO tropical convection.

12.4 Impacts of El Niño–Southern Oscillation

12.4.1 Phase residence time

ENSO’s influence on the phase residence time of the MJO or GWO can be determined by using data with only the annual cycle removed. Our RMM is thus different from Wheeler and Hendon⁵³ in that ENSO or a 120-day running mean is retained. The GWO index also retains all temporal variability. To differentiate between indices, we refer to our indices as RMM_all and GWO_all. When using these indices, subseasonal phases are favored or avoided depending on

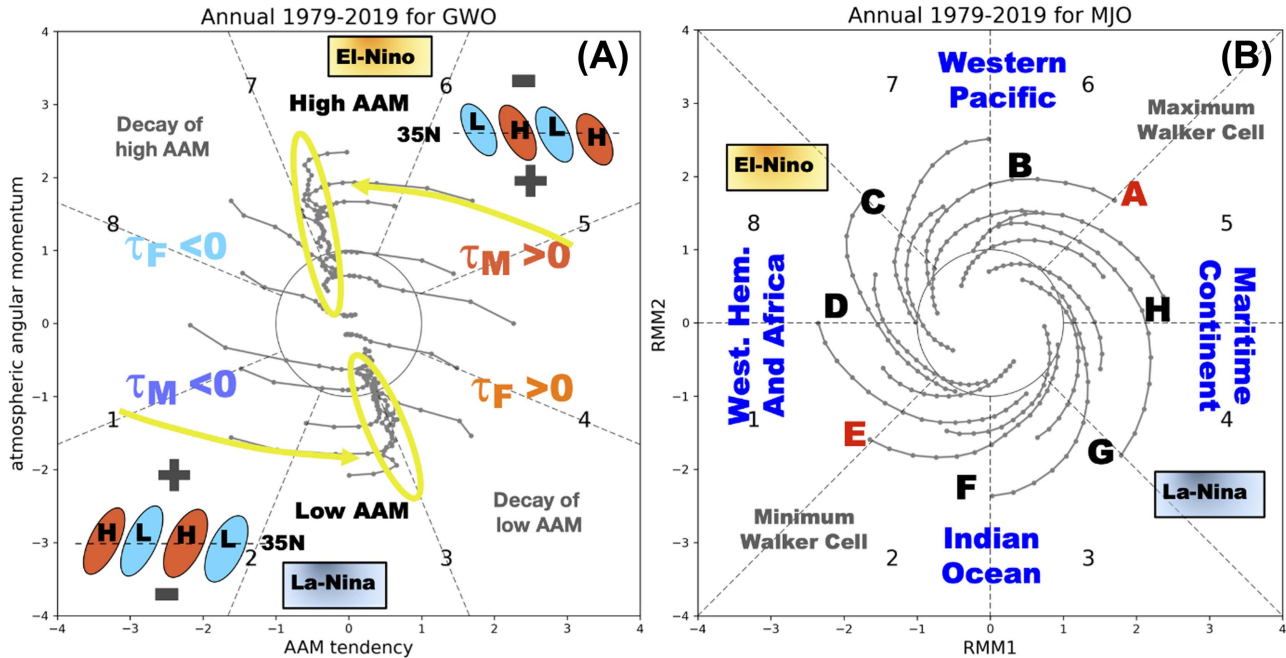


FIGURE 12.8 Madden–Julian Oscillation (MJO) and Global Wind Oscillation (GWO) phase spaces. (A) The GWO phase space, where annotations include (1) lag trajectories that start from 16 phases and go out to 15 days, (2) phase location and a sign of global mountain and friction torque anomalies, and (3) phase location of zonal mean AAM transports across 35° N with schematic eddy tilts that contribute to the transports. The lag trajectories are for annual data during 1979–2019. A rapid rise of negative or positive AAM anomalies (yellow arrows) is followed by a slow decay in phase 3 or 7 (yellow stretched ovals). (B) The MJO phase space, where annotations include (1) the geographic location of tropical convection, (2) lag trajectories as in (A), and (3) lettered phases used by Madden and Julian⁵⁴ where phase A (E) has the maximum (minimum) Walker Cell. The autoregressive character of the lag trajectories in (A) contrasts with the quasi-oscillatory ones seen in (B).

ongoing El Niño or La Niña conditions. An excellent proxy for ENSO is global AAM.^{14,17,52,56} It is well known that high global AAM occurs during El Niño and low AAM during La Niña.^{14,57}

Fig. 12.9 shows a composite of RMM_all phase residence times for seasons with a positive (red lines) or negative (blue lines) global AAM anomaly of >0.5 or $<-0.5 \sigma$. There is a clear divide in the preferred residence time between the red and blue lines. Large fractional values occur in phases 3–4 during low AAM or La Niña (blue lines) while they occur in phases 6–7–8 during high AAM or El Niño (red lines). Seasonal evolution is also exhibited especially with El Niño where maxima shift toward the Indian Ocean during boreal summer and back again to the Maritime Continent during boreal fall. The frequency differences, when compared with an expected value of 8% per phase, range from $>25\%$ in phase 3 during La Niña DJFs to $<2\%$ in phases 1–2 during El Niño ASOs and La Niña JJAs. These represent 23 days and 2 days per season, respectively, compared with the expected 7 days. The expected value of 8% per phase comes from compositing on an index value of 1σ where approximately 64% of the data are used (over 8 phases), thus $64\%/8 = 8\%$.

A similar analysis to Fig. 12.9, but focusing on DJF and using Niño 3.4 SSTs to define ENSO, is shown in Fig. 12.10. The red and blue dashed lines are for GWO_all where the phase has been shifted forward (i.e., counterclockwise) by 1 phase. These correspond nicely to the RMM_all results for El Niño and La Niña. The upper portion of the GWO phase space (Fig. 12.8A) is preferred during El Niño while the lower portion is populated during La Niña. The heavy black line is the average residence time based on 15 different analyses that include eight performed by us, four by Lee et al.⁵⁸ and three by Fernandes and Grimm.⁵⁹ The studies include different time periods, different ENSO phases, different ENSO indices, different modes (RMM, RMM_all, OLR-based MJO index, and RMM_c which is a 120-day centered version of the RMM) and slightly different months (NDJFM versus DJF).

The signal with the dominant ENSO impact removed is relatively small with maxima at phases 3 and 7 and a minimum at phase 1. These signals were explored in considerable detail by Lee et al.,⁵⁸ Fernandes and Grimm,⁵⁹ and others who used the RMM. They are real and represent phases on the opposite side of the ENSO signal (e.g., phases 3–4 during El Niño and phase 7 during La Niña) where persistent ENSO anomalies disrupt the MJO signal typically associated with these phases (cf. Fig. 3b from Ref. 58). The signal comes from removing ENSO, which shifts the phase space

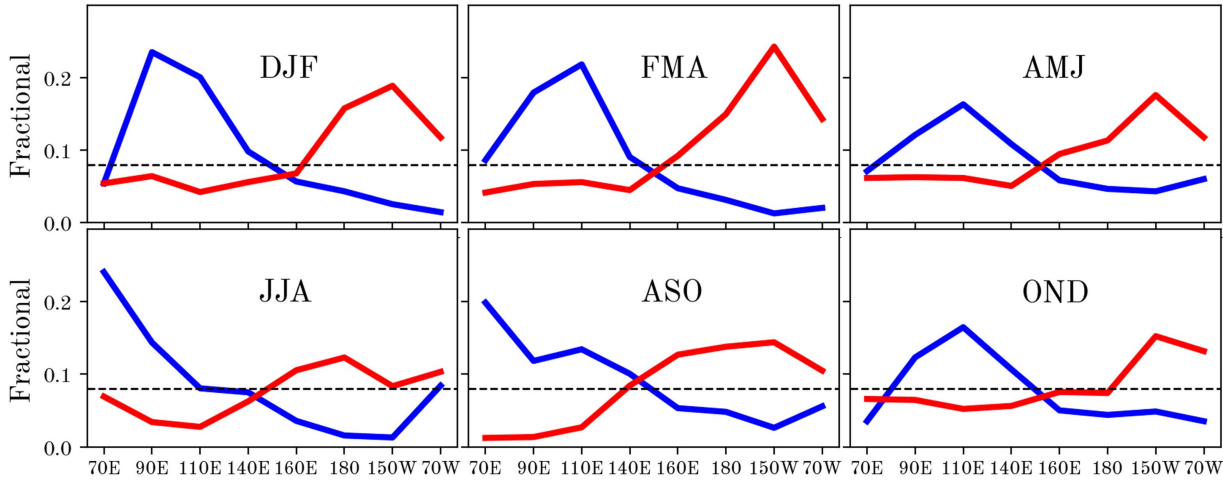


FIGURE 12.9 A composite of RMM_all phase residence times for seasons with a positive (red lines) or negative (blue lines) global AAM anomaly of >0.5 or $<-0.5 \sigma$. There is a clear divide in the preferred residence time between the red and blue lines. Large fractional values occur in phases 3–4 during low AAM or La Niña (blue lines) while they occur in phases 6–7–8 during high AAM or El Niño (red lines). Seasonal evolution is also exhibited especially with El Niño where maxima shift toward the Indian Ocean during boreal summer and back again to the Maritime Continent during boreal fall. The frequency differences, when compared with an expected value of 8% per phase, range from $>25\%$ in phase 3 during La Niña DJFs to $<2\%$ in phases 1–2 during El Niño ASOs and La Niña JJAs.

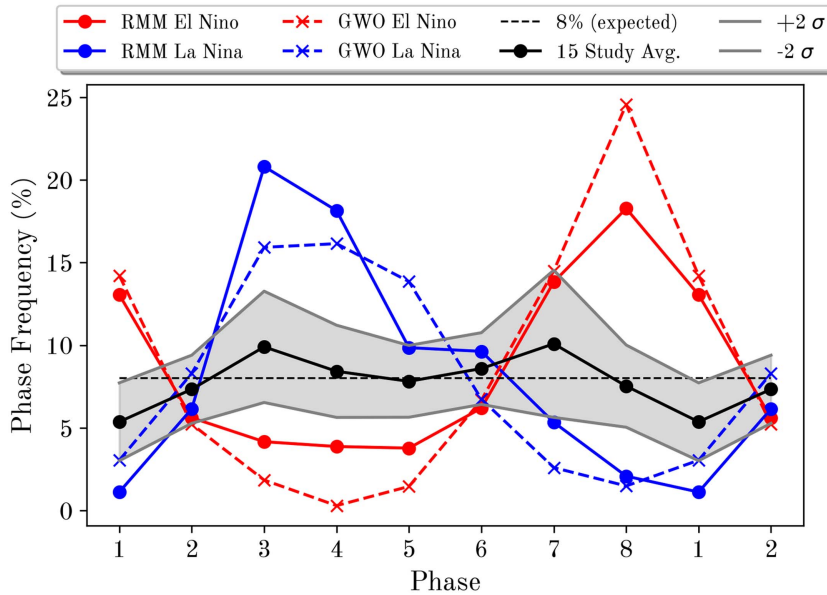


FIGURE 12.10 The frequency of occurrence for eight phases (two repeated) of GWO/MJO during different ENSO conditions. The solid blue (red) lines are for La Niña (El Niño) using RMM_all; the dashed lines are the same but for the GWO. The solid black line is the average frequency of occurrence for 15 different studies that in some way remove the primary ENSO signal. The shading is the $\pm 2 \sigma$ limits of the mean. The dashed black line is the 8% expected value of the frequency.

mean back toward zero and populates phases opposite to the main ENSO impact phases shown in Fig. 12.10. Utilizing 15-day lags allows one to capture portions of the main ENSO signal that are missed at day 0 when using the RMM (cf. Fig. 1b from Ref. 58).

12.4.2 Phase space trajectory

A logical effort would be to combine the MJO and GWO into a single phenomenon where tropical convection, global torques, and other processes all contribute to the intraseasonal evolution of anomalies. A preliminary attempt is described in this section where a quasi-3-D phase space is introduced. The phase space consists of RMM1 and RMM2 as the x and y coordinates and global AAM as the z coordinate. The space is “quasi” because the coordinates are not independent variables in that global AAM is correlated with RMM1.¹⁷ The results describe average behavior over

DJF 1979-2019 GWO El Niño (red, 4.5-7.5) | La Niña (blue, 0.5-4.5)

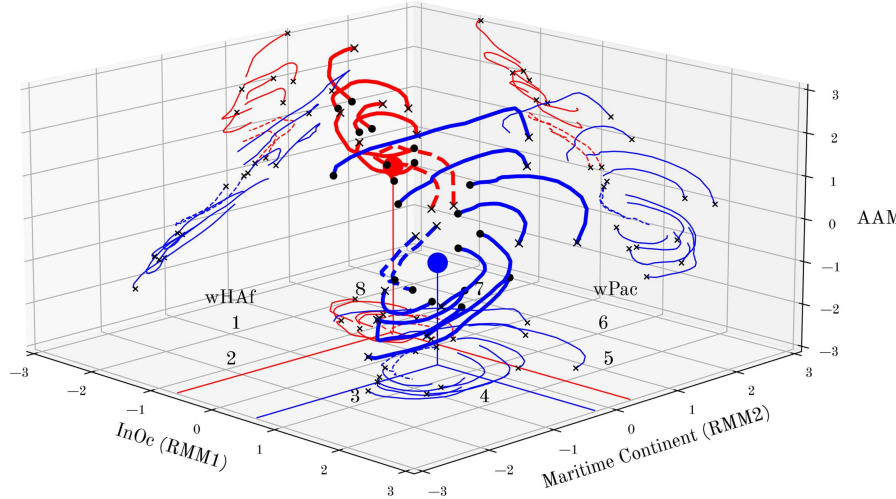


FIGURE 12.11 Fifteen-day lagged trajectories (thick lines) using the GWO_all index in the (RMM1, RMM2, AAM) space. Trajectories emanate from selected phases for El Niño (red) and La Niña (blue), with the start (end) marked by a “ \times ” (dot). The red and blue dots are the El Niño and La Niña mean in the phase space. The thin lines are the projection of the 3-D trajectories onto the $x-y$, $y-z$, and $x-z$ planes, with the start marked by a “ \times ”. The $x-y$ plane represents the RMM phase space. The trajectories circle counterclockwise. The dashed blue/red trajectory represents phase 4.5 for El Niño or phase 0.5 for La Niña, the start of the phase sequence shown in the figure. Results are for DJF, 1979–2019. ENSO was defined using Niño 3.4 SST.

12–15 DJF seasons that are flagged as El Niño or La Niña. Sampling is always a concern, especially since aspects of El Niño are known to have changed during the 1979–2019 period.

12.4.2.1 GWO_all index

The 2-D GWO phase space (Fig. 12.8) only has one degree of freedom: if you know global M_R , you know its tendency ($\frac{dM_R}{dt}$). This carries over to the 3-D trajectories presented in this section. When they are projected onto the vertical $x-z$ and $y-z$ planes, they provide information about the sign of the global tendency and can differentiate between the mountain and frictional torques. Any “vertical motion” must be due to a torque. The sign is determined from the CCW rotation of lagged trajectories and whether the projected lines move up or down with lag in the vertical plane. The type of torque comes from the trajectory’s slope. Steep, short slopes flag the mountain torque and long, shallow slopes flag the frictional torque. A mixture of the two with moderate slopes can also be seen. The torque separation is related to the separation in their spectra seen in Fig. 12.7 (see also Ref. 33). Adding the two degrees of freedom from RMM1 and RMM2 links the trajectories in the 2-D GWO space to tropical convection and 200/850 hPa zonal wind.

Fig. 12.11 depicts the 3-D phase space trajectories using GWO_all to determine the trajectories. The figure includes only those trajectories that have high residence times during La Niña (blue) and El Niño (red). The $x-y$, $y-z$, and $x-z$ projections are shown on the $z = -3$, $x = -3$, and $y = +3$ surfaces for ease of viewing although they belong centered around the respective El Niño and La Niña means (the red and blue dots). To understand the links correctly, the trajectories should be mentally transported to these locations.

Two distinct 2-D surfaces are seen. During El Niño (red thick lines), the surface slopes upward toward the $y-z$ plane to high AAM and eastern Pacific tropical convection anomalies. The trajectories tend to curve counterclockwise toward the El Niño mean of high AAM and tropical eastern Pacific convection. During La Niña (blue thick lines) the surface slopes upward toward the $x-z$ plane and the trajectories more coherently circle the La Niña mean of low AAM and Maritime Continent convection.

The projection into the horizontal $x-y$ plane provides information on the MJO and its eastward propagation through the familiar 2-D RMM phase space^a (e.g., Fig. 12.8). It also reveals the link between the GWO torques and the MJO convection and winds during ENSO. La Niña projections are broader and cover more area than the El Niño counterpart. The blue-colored trajectories move through phases 3–4–5–6^b representing tropical convection^c going from the Indian Ocean to the western Pacific Ocean. El Niño projections are relatively truncated and spiral into the mean with a long axis that extends to eastern Pacific convection. The red-colored trajectories move eastward from the western Pacific (via Western Hemisphere/Africa, hereafter wHAf) to the Indian Ocean but hardly at all toward the Maritime Continent.

a. The trajectories are relative to the El Niño and La Niña means. Thus, referring to a specific phase in the RMM space is relative to these means. For example, relative to the La Niña mean that sits in RMM phase 3–4, the opposite RMM phases 7–8 may have zero anomaly depending on the standard deviation of an event’s projection.

b. Here and following we refer to the RMM phases. Physically the RMM and GWO phases differ by 1.5 phases.

c. The RMMs consist of a combination of OLR and 850 and 200 hPa zonal wind.

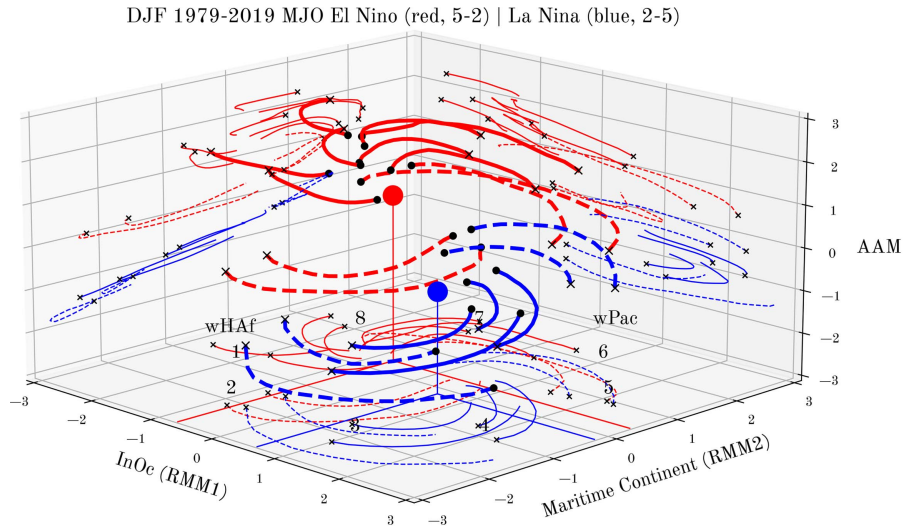


FIGURE 12.12 As in Fig. 12.11 but using RMM_all as the compositing index. The dashed trajectories are for contrasting between El Niño and La Niña; see text for details.

During La Niña, an oscillatory vertical structure is evident in the low AAM portion of the $x-z$ plane. During El Niño, it occurs in the high AAM portion of the $y-z$ plane. The La Niña oscillation is linked with a circuit in RMM phase space during which the friction and mountain torques drive AAM up and then down. A positive (negative) T_M occurs with convection over the Maritime Continent (wHAF); these are the strong vertical branches of the oscillation. The horizontal branches hint at a negative friction torque leading to the negative T_M and vice versa. Overall, the structure provides an illustration of the friction-mountain torque index cycle discussed earlier.

A more persistent positive/negative T_F is illustrated by the sloped lines in the $y-z$ plane. They are positive and moving upward through phases 3–6, and negative and moving downward through phases 7–2. These linkages are seen more clearly for the downward branch whose trajectories are dashed in all three planes and can be tracked more easily. The downward branch is linked to a negative T_M and relative wHAF convection anomalies. A negative T_F occurs with convection over the wHAF and while moving into the Indian Ocean region.

During El Niño, the oscillatory structure is less expansive. The upward branch denotes a positive T_M that occurs with dateline convection and the downward branch denotes a negative T_M related to Indian Ocean convection. Again, these are relative to the El Niño mean centered in phase 8. At the same time, in the $x-z$ plane, the thin red lines denote positive and negative frictional torques that are linked with Maritime Continent and wHAF convection anomalies. The dashed trajectory shows a mostly steady positive torque and increase in AAM before falling back to the El Niño mean in the $x-z$ and $y-z$ planes.

Some trajectories in the vertical planes of Fig. 12.11 have a hooked-shaped appearance as also noted in Fig. 12.8. These represent trajectories that go through phase 2.5 or 6.5 in the GWO phase space, which occur when torques are zero and AAM reaches a minimum or maximum. The “hook” pulls back on the ongoing AAM change through negative feedback from the frictional torque.

The distinct separation of El Niño and La Niña trajectories in Fig. 12.11 implies a change in the relationship between AAM and the RMM is induced by ENSO. It contrasts with the single 2-D surface obtained when analyzing MJOs or GWOs under neutral ENSO conditions. For the GWO, a single surface tilts up toward phases 7–8 (not shown) and its interpretation is decidedly simpler than the separate ENSO ones. On the other hand, the results when using all years to produce the trajectories is a linear combination of the El Niño and La Niña years. These should not be used when seeking “inherent” MJO composites separate from ENSO. Rather, the neutral years are a better choice.⁶⁰ In the next section, the 3-D trajectories are presented when RMM_all is used to make the composites instead of GWO_all.

12.4.2.2 RMM_all index

Fig. 12.12 is the 3-D phase diagram using the RMM_all index to determine its three components. The trajectories mostly include ones with high residence time although the two dashed red and two dashed blue trajectories for phase 2 (left side of figure) and similarly for phase 5 (right side of figure) are included to contrast El Niño (red) and La Niña (blue) induced movement. Overall, there are similarities with Fig. 12.11. For example, trajectories circle *around* the La Niña mean and *into* the El Niño mean just as with the GWO. However, in general the trajectories are more sweeping

and the 2-D surface tilts are weaker (albeit in a similar direction). There is an interesting lack of connection between the red phase 1 (solid) and red phase 2 (dashed) on the left side of the figure. We speculate the persistence of high AAM makes it difficult to start a new event over the Indian Ocean during El Niño.

The projection onto $x-y$ horizontal plane depicts the RMM space (Fig. 12.8B). The red and blue dashed trajectories emanating from phase 2 and phase 5 contrast the eastward propagation between El Niño and La Niña. The El Niño trajectories propagate faster through the Indian and western Pacific region than the La Niña ones. The vertical projections have similar features to the GWO including remnants of a vertical oscillation for both La Niña ($x-z$ plane lower right) and El Niño ($y-z$ plane upper right), although only the upward vertical branch is evident. There is a hint of a downward branch (negative T_M) during El Niño phase 1 in the $y-z$ plane, but it is otherwise missing since there are no intervening phases for 1/8 cycle resolution. An erratic downward vertical branch during La Niña occurs at phase 7 (not shown). Overall, the torques are weaker as indicated by the shallower slope of the sloped, straight lines at the bottom of the $y-z$ plane (blue) and the top of the $x-z$ plane (red), and by the weaker upward component during La Niña in the $x-z$ plane.

So far, the primary focus has been on the relationship between regional tropical convection (200–850 hPa zonal wind), the global AAM, and the associated torques. Compositing different variables is one way to further explore the link between a global index and the global circulation. In the next section, 200 hPa streamfunction (ψ) is used to help regionalize some of the features discussed with regard to Fig. 12.12. We focus on RMM_all—rather than GWO_all—because we want to further compare results with Lee et al.⁵⁸ and Fernandes and Grimm.⁵⁹

12.4.3 200 hPa streamfunction

Fig. 12.13 displays the 200 hPa ψ standardized anomalies for all eight phases of the MJO based on RMM_all during El Niño (left) and La Niña (right). These maximize at phases 7–8 for El Niño (Fig. 12.13G and H) and phases 3–4 during La Niña (Fig. 12.13K and L). For El Niño, westerly flow develops in the tropics of the Western Hemisphere during phase 5, and by phase 8 encompasses most of the tropics along with deep westerly flow in the midlatitudes of the Pacific Ocean. Nearly the opposite scenario unfolds during La Niña (Fig. 12.13I–L).

By using the RMM instead of RMM_all, Lee et al.⁵⁸ and Fernandes and Grimm⁵⁹ concentrate their analysis on phases 3–4 during El Niño and phase 7 during La Niña. These represent periods where a transition to tropical easterlies and lower AAM occurs during El Niño and a transition to tropical/subtropical westerlies and higher AAM occurs during La Niña. Note that these phases are opposite to those preferred during El Niño and La Niña, and, indeed, have a low number of days recorded in Fig. 12.13. However, that changes when the original RMM is used and the mean ENSO signal is removed. Phases 3–4 during El Niño (Fig. 12.13C and D) now contain 114 and 110 days, respectively, whereas phases 6–7 during La Niña contain 134 and 204 days, respectively. The patterns also change, but not substantially (not shown). This secondary signal is the primary contributor to the results shown in Fig. 12.10 (black solid line). It is a real ENSO signal but has smaller phase frequencies than the dominant ENSO signal obtained when using RMM_all.

To summarize, the 15-day lagged trajectories in vertical planes of the 3-D phase space (Fig. 12.11) consist of vertical oscillations, sloped vertical movements up/down and the “hooked” sequences. ENSO organizes these features into distinct regions of the 3-D space. The strongest torques, generally mountain torques, are linked with Maritime Continent and wHAf convection during La Niña and western Pacific and Indian Ocean convection during El Niño. This change is likely related to the different El Niño and La Niña base states combined with the location of the major mountain ranges. Overall, the GWO drives a weak tropical convective signal while the MJO drives a moderate torque signal. Next, we present evidence from an individual case that the GWO can drive tropical convection.

12.5 Example case study (March 28–May 26, 2007)

This case was originally studied by Weickmann and Berry¹⁷ who focused on large positive and negative global AAM tendencies within two ≈ 30 -day oscillations of the GWO. The MJO, as measured by the RMM, was only sporadically active and the stronger RMM projections were attributed to GWO forcing. The case was chosen because the GWO was more coherent than the MJO, the period represented the onset of the 2007–2008 La Niña, and it is a representative sample from the 1999–2023 La Niña-like climate state.⁶¹ In this update, we focus on the poleward propagation of zonal AAM anomalies contrasting a rapid event early in the period with a much slower one later.

Two prominent GWO orbits in the phase plot were noted for this period (Fig. 12.14A). The first (red line) is a broad single orbit that has a large positive tendency and a moderate long-lived negative tendency, while the second combines a slow and fast orbit. On average, the orbits are centered away from zero toward phases 3–4 signifying negative global AAM anomalies characteristic of a La Niña circulation state. Simultaneously, Niño 3.4 SST anomalies decreased from

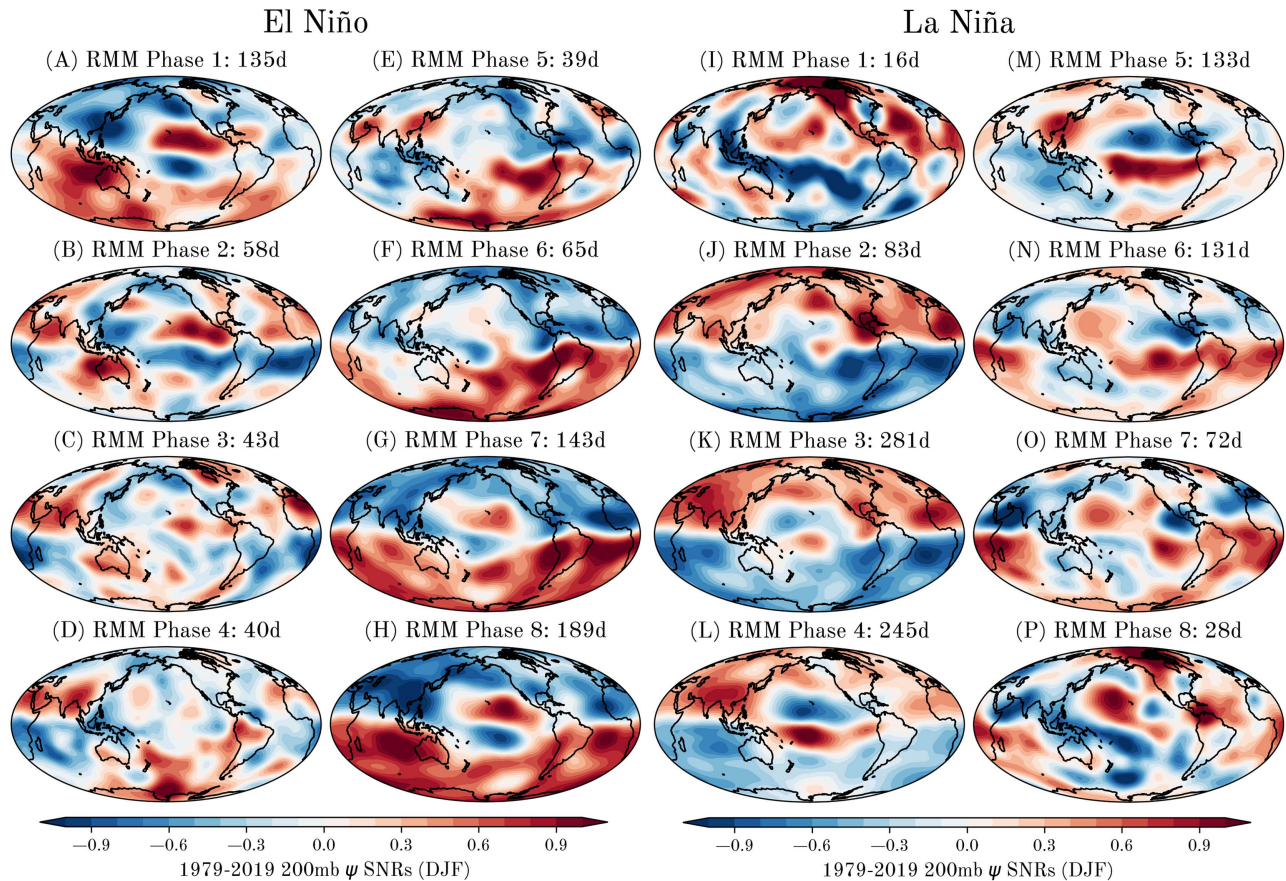


FIGURE 12.13 200 hPa streamfunction (ψ) standardized anomalies for eight phases of the MJO (RMM) for (A–H) El Niño and (I–P) La Niña. Blue (red) anomalies in the Northern Hemisphere (Southern Hemisphere) are times of high AAM during El Niño such as panels E–H. The opposite colors flag low AAM during La Niña such as panels J–L. The days in each phase labeled are from a total of 1300 La Niña and 1000 El Niño days, respectively. Map lines delineate study areas and do not necessarily depict accepted national boundaries.

+0.7 to −0.5 from January to May 2007. The regularity of the GWO orbits contrasts with the more variable MJO projections (Fig. 12.14B). Brief flareups in certain phases combine with long periods of weak projection. Weickmann and Berry¹⁷ speculated the flareups were initiated by the GWO through trade wind fluctuations and pressure surges related to mountain torques.

The MJO circuits are not unlike the El Niño and La Niña projections on the RMM phase space obtained in Fig. 12.11. In fact, Niño 3.4 SSTs were trending negative during April–May 2007 and AAM was already low. The excursion at the end of the period represents a shift toward El Niño in the RMM, although the GWO ends with a -1σ AAM anomaly. This could represent a weak version of the MJO phase 7 La Niña signal discussed earlier with regard to Fig. 12.10.

Fig. 12.15 depicts the global and zonal M_R anomalies for the period while Fig. 12.16 shows the M_R tendencies. Recall that the GWO phase space plot (Fig. 12.14A) is constructed from standardized anomalies of the two global time series in Fig. 12.15B and 12.16B. The red line on both global time series follows the first orbit while the blue line follows the second.

The first orbit is preceded by a northward transport of M_R that is annotated in Figs. 12.15 and 12.16. It provides a good illustration of a strong, coherent signal in the right place to initiate an orbit. Generally, the transport patterns have more complicated or noisy meridional structures as can be seen in Fig. 12.16; however, they represent the largest forcing in the zonal M_R budget and are approximately equal to the sum of all the torques.

Fig. 12.15A shows the effect of the first orbit on the zonal M_R anomalies. The strong rise in M_R is realized as enhanced westerly flow around 35°N and weakened easterly anomalies to the north (45°N) and south (10°N). The superimposed line implies a poleward movement of the M_R tendency from near the equator to about 50°N. The line is also superimposed on the tendency field in Fig. 12.16A, which is more episodic but provides continuity for the poleward transport of M_R .

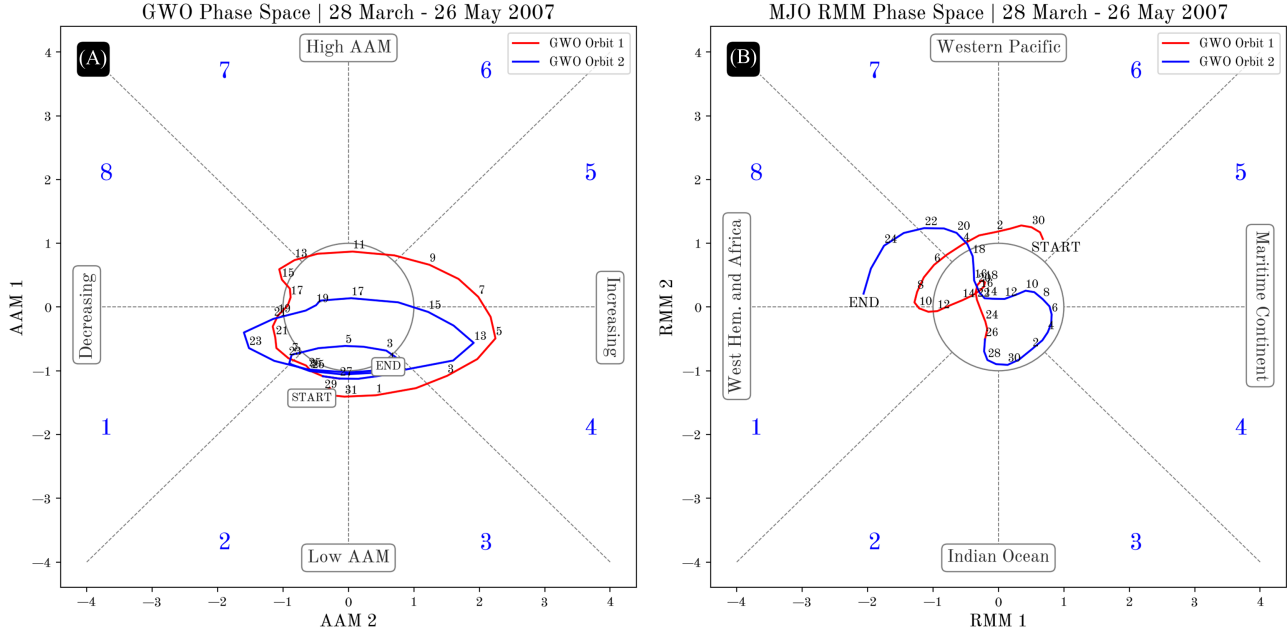


FIGURE 12.14 (A) The GWO and (B) MJO RMM phase space plot for the case in March 28–May 25, 2007. In both (A) and (B) the red line is the first GWO orbit and the blue line is the second.

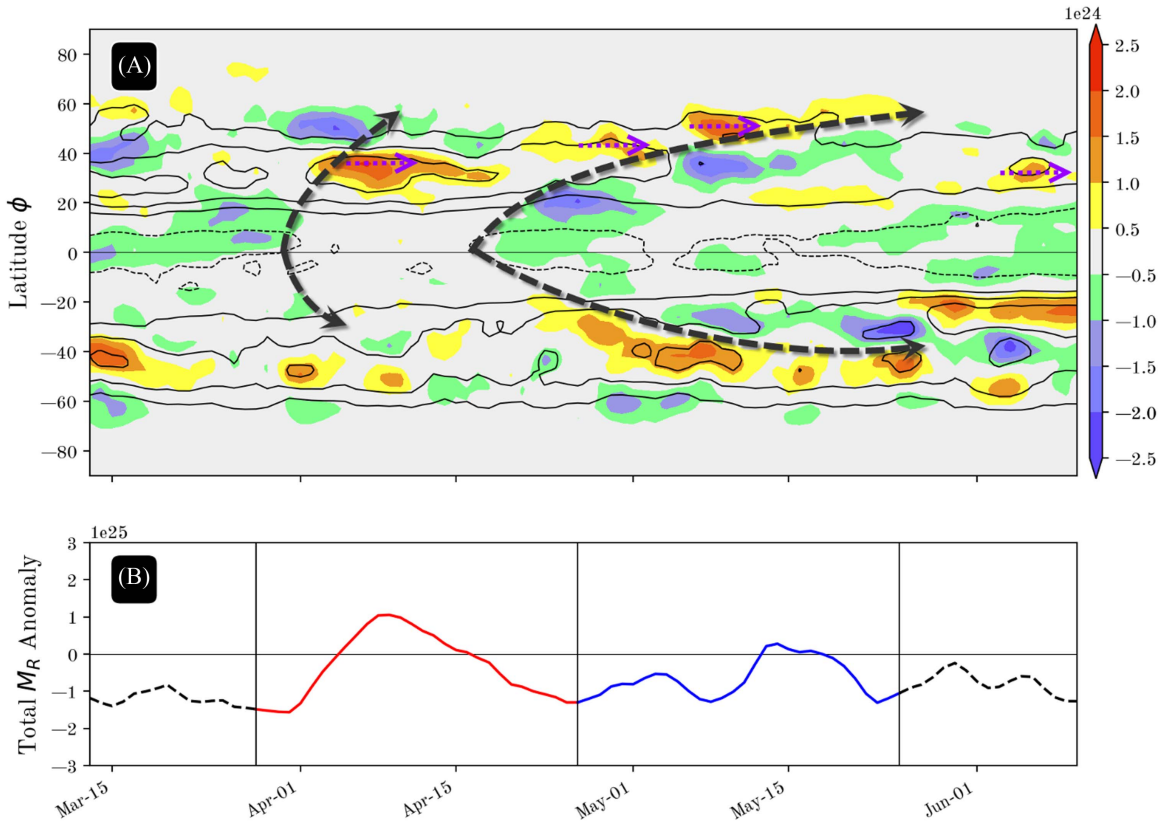


FIGURE 12.15 (A) The zonal M_R anomaly as a function of latitude and time for a 90-day period that includes the case study. Contours show the total zonal AAM with a contour interval of $2.0 \times 10^{24} \text{ kg} \cdot \text{m}^2/\text{s}$, while the shading indicates positive and negative anomalies. Thick dashed arrow annotations show the poleward movement of positive AAM tendencies during the first orbit, and of negative tendencies during the second orbit. Purple dashed arrows emphasize locations of westerly wind anomalies. (B) The global total M_R anomaly, where the vertical lines and different colors bound the first and second orbits as previously shown in Fig. 12.14.

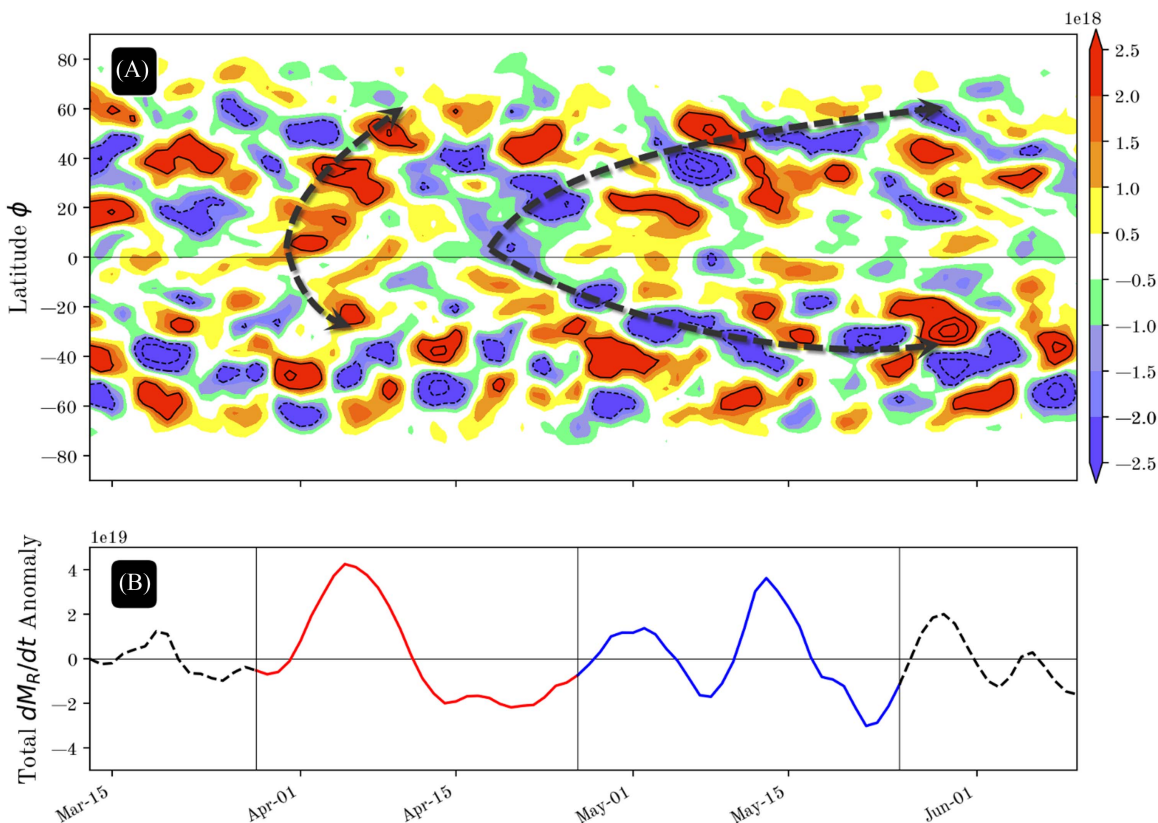


FIGURE 12.16 (A) As in Fig. 12.15A, but for the zonal M_R tendency. The postulated poleward movements of a positive and a negative tendency are highlighted by dashed black arrows. (B) As in Fig. 12.15B, but for the global total M_R tendency.

The large negative tendency in late April within 10°S – 30°N coincides with the negative phase of orbit 1 and initiates a slower poleward moving negative tendency towards higher latitudes of both hemispheres. The second orbit with slow and fast components basically keeps M_R low as the La Niña circulation response consolidates into its weakened jet stream state. Another period of lower M_R develops in late May 2007 between 10°S and 20°N , eventually leading to persistent negative M_R anomalies in the subtropics of both hemispheres during boreal summer/fall 2007.

The emphasis on poleward movement of M_R anomalies in the case study highlights this much-studied feature of the climate. We estimated movement values from 2 to 5 m/s on subseasonal time scales, whereas on interannual the order is closer to 0.1 m/s. These forced features of the circulation could provide predictability of (at least) averaged flows.²⁵ Further investigations using multivariate linear regression and machine learning methods may tease out the poleward propagating behavior from noisy data. Additional commentary on this case study is presented in Weickmann and Berry.¹⁷

12.6 A tribute to Edward (Ed) Berry

Edward (Ed) Berry was born to be a meteorologist. He loved to analyze and diagnose severe weather outbreaks and synoptic storms in the westerlies. But his true love was on the global scale and how the daily weather noise gives rise to slow climate variations that might be predictable. And prediction was the name of the game for Ed, and his forte. He routinely made skillful predictions out to 2–3 weeks. When the forecasts were analyzed, the skill only came out after a systematic error was removed; namely, a trough in the western United States—Ed's favorite weather pattern. After all, he grew up in Iowa and the weather gets your attention there.

Ed's career was marked by distinguished service in the National Weather Service and significant roles in the private sector. It reflects a blend of public service dedication and private sector innovation that Ed was always striving for. His work bridged the often-divergent worlds of governmental research and commercial application, showcasing his unique ability to translate complex atmospheric phenomena into practical, actionable insights.

Beyond his scientific contributions, Ed was a mentor and an inspiration to many. His passion for meteorology was not just in the pursuit of knowledge, but in sharing that knowledge, fostering a community of inquisitive minds dedicated to unraveling the mysteries of the atmosphere. We remember him in the ever-shifting winds, in the sprawling synoptic charts, in the daily 10-page weather discussions and much more. But we also remember him as a good person who loved his family, friends, long walks, and life.

References

- Starr VP. An essay on the general circulation of the Earth atmosphere. *Journal of Meteorological Research*. 1948;5(2):39–43. Available from: [https://doi.org/10.1175/1520-0469\(1948\)005<0039:aeotgc>2.0.co;2](https://doi.org/10.1175/1520-0469(1948)005<0039:aeotgc>2.0.co;2).
- Starr VP, White RM. A hemispherical study of the atmospheric angular-momentum balance. *Quarterly Journal of the Royal Meteorological Society*. 1951;77(332):215–225. Available from: <https://doi.org/10.1002/qj.49707733206>.
- Lorenz E. *The Nature and Theory of the General Circulation of the Atmosphere*. World Meteorological Organization; 1967.
- Oort AH. Angular momentum cycle in the atmosphere-ocean-solid Earth system. *Bulletin of the American Meteorological Society*. 1989;70(10):1231–1242. Available from: [https://doi.org/10.1175/1520-0477\(1989\)070<1231:amcta>2.0.co;2](https://doi.org/10.1175/1520-0477(1989)070<1231:amcta>2.0.co;2).
- Rosen RD. The axial momentum balance of Earth and its fluid envelope. *Surveys in Geophysics*. 1993;14(1):1–29. Available from: <https://doi.org/10.1007/BF01044076>.
- Egger J, Weickmann K, Hoinka KP. Angular momentum in the global atmospheric circulation. *Reviews of Geophysics*. 2007;45(4):RG4007. Available from: <https://doi.org/10.1029/2006RG000213>.
- Barnes RTH, Hide R, White AA, Wilson CA. Atmospheric angular momentum fluctuations, length-of-day changes and polar motion. *Proceedings of the Royal Society of London. Series A, Mathematical and Physical Sciences*. 1983;387(1792):31–73.
- Bell MJ, Hide R, Sakellarides G. Atmospheric angular momentum forecasts as novel tests of global numerical weather prediction models. *Philosophical Transactions of the Royal Society A: Mathematical, Physical and Engineering Sciences*. 1991;334(1633):55–92. Available from: <https://doi.org/10.1098/rsta.1991.0003>.
- Black RX, Salstein DA, Rosen RD. Interannual modes of variability in atmospheric angular momentum. *Journal of Climate*. 1996;9(11):2834–2849. Available from: [https://doi.org/10.1175/1520-0442\(1996\)009<2834:IMOVIA>2.0.CO;2](https://doi.org/10.1175/1520-0442(1996)009<2834:IMOVIA>2.0.CO;2).
- Chao BF. Length-of-day variations caused by El Niño Southern Oscillation and Quasi-Biennial Oscillation. *Science*. 1989;243(4893):923–925. Available from: <https://doi.org/10.1126/science.243.4893.923>.
- Dickey JO, Marcus SL, Steppe JA, Hide R. The Earth's angular momentum budget on subseasonal time scales. *Science*. 1992;255(5042):321–324. Available from: <https://doi.org/10.1126/science.255.5042.321>.
- Krishnamurti TN, Sinha MC, Krishnamurti R, Oosterhof D, Comeaux J. Angular momentum, length of day and monsoonal low frequency mode. *Journal of the Meteorological Society of Japan. Ser. II*. 1992;70(1B):131–166. Available from: https://doi.org/10.2151/jmsj1965.70.1b_131.
- Rosen RD, Salstein DA. Contribution of stratospheric winds to annual and semiannual fluctuations in atmospheric angular momentum and the length of day. *Journal of Geophysical Research*. 1985;90(5):8033–8041. Available from: <https://doi.org/10.1029/JD090iD05p08033>.
- Rosen RD, Salstein DA, Eubanks TM, Dickey JO, Steppe JA. An El Niño signal in atmospheric angular momentum and Earth rotation. *Science*. 1984;225(4660):411–414. Available from: <https://doi.org/10.1126/science.225.4660.411>.
- Salstein DA, Rosen RD. Earth rotation as a proxy for interannual variability in atmospheric circulation, 1860–present. *Journal of Applied Meteorology and Climatology*. 1986;25(12):1870–1877. Available from: [https://doi.org/10.1175/1520-0450\(1986\)025<1870:ERAAPP>2.0.CO;2](https://doi.org/10.1175/1520-0450(1986)025<1870:ERAAPP>2.0.CO;2).
- Weickmann KM, Sardeshmukh PD. The atmospheric angular momentum cycle associated with a Madden–Julian oscillation. *Journal of the Atmospheric Sciences*. 1994;51(21):3194–3208. Available from: [https://doi.org/10.1175/1520-0469\(1994\)051<3194:taamca>2.0.co;2](https://doi.org/10.1175/1520-0469(1994)051<3194:taamca>2.0.co;2).
- Weickmann K, Berry E. The tropical Madden–Julian Oscillation and the Global Wind Oscillation. *Monthly Weather Review*. 2009;137(5):1601–1614. Available from: <https://doi.org/10.1175/2008MWR2686.1>.
- Weickmann KM, Khalsa SJS, Eischeid J. The atmospheric angular-momentum cycle during the tropical Madden–Julian oscillation. *Monthly Weather Review*. 1992;120(10):2252–2263. Available from: [https://doi.org/10.1175/1520-0493\(1992\)120<2252:TAAMCD>2.0.CO;2](https://doi.org/10.1175/1520-0493(1992)120<2252:TAAMCD>2.0.CO;2).
- Xu XQ, Zhou YH, Duan PS, et al. Contributions of oceanic and continental AAM to interannual variation in Δ LOD with the detection of 2020–2021 La Niña event. *Journal of Geodesy*. 2022;96(6):43. Available from: <https://doi.org/10.1007/s00190-022-01632-x>.
- Boer GJ. Earth-atmosphere exchange of angular momentum simulated in a general circulation model and implications for the length of day. *Journal of Geophysical Research*. 1990;95(5):5511–5531. Available from: <https://doi.org/10.1029/JD095iD05p05511>.
- Eubanks TM, Steppe JA, Dickey JO, Callahan PS. A spectral analysis of the Earth's angular momentum budget. *Journal of Geophysical Research: Solid Earth*. 1985;90(B7):5385–5404. Available from: <https://doi.org/10.1029/jb090ib07p05385>.
- Hide R, Birch NT, Morrison LV, Shea DJ, White AA. Atmospheric angular momentum fluctuations and changes in the length of the day. *Nature*. 1980;286(5769):114–117. Available from: <https://doi.org/10.1038/286114a0>.
- Langley RB, King RW, Shapiro II, Rosen RD, Salstein DA. Atmospheric angular momentum and the length of day: A common fluctuation with a period near 50 days. *Nature*. 1981;294(5843):730–732. Available from: <https://doi.org/10.1038/294730a0>.
- Salstein DA, Rosen RD. Topographic forcing of the atmosphere and a rapid change in the length of day. *Science*. 1994;264(5157):407–409. Available from: <https://doi.org/10.1126/science.264.5157.407>.
- Scaife AA, Hermanson L, van Niekerk A, et al. Long-range predictability of extratropical climate and the length of day. *Nature Geoscience*. 2022;15(10):789–793. Available from: <https://doi.org/10.1038/s41561-022-01037-7>.

26. Madden RA, Speth P. Estimates of atmospheric angular momentum friction, and mountain torques during 1987–1988. *Journal of the Atmospheric Sciences*. 1995;52(21):3681–3694. Available from: [https://doi.org/10.1175/1520-0469\(1995\)052<3681:EOAAMF>2.0.CO;2](https://doi.org/10.1175/1520-0469(1995)052<3681:EOAAMF>2.0.CO;2).
27. Kalnay E, Kanamitsu M, Kistler R, et al. The NCEP/NCAR 40-year reanalysis project. *Bulletin of the American Meteorological Society*. 1996;77(3):437–471. Available from: [https://doi.org/10.1175/1520-0477\(1996\)077<0437:TNYRP>2.0.CO;2](https://doi.org/10.1175/1520-0477(1996)077<0437:TNYRP>2.0.CO;2).
28. Peixoto JP, Oort AH. *Physics of Climate*. AIP Publishing; 1992. Available from: <https://doi.org/10.1063/1.2809772>.
29. Huang HP, Sardeshmukh PD. Another look at the annual and semianual cycles of atmospheric angular momentum. *Journal of Climate*. 2000;13(18):3221–3238. Available from: [https://doi.org/10.1175/1520-0442\(2000\)013<3221:ALATAA>2.0.CO;2](https://doi.org/10.1175/1520-0442(2000)013<3221:ALATAA>2.0.CO;2).
30. Kang I-S, Lau KM. Principal modes of atmospheric circulation anomalies associated with global angular momentum fluctuations. *Journal of the Atmospheric Sciences*. 1994;51(9):1194–1205. Available from: [https://doi.org/10.1175/1520-0469\(1994\)051<1194:pmoaca>2.0.co;2](https://doi.org/10.1175/1520-0469(1994)051<1194:pmoaca>2.0.co;2).
31. Rosen RD, Salstein DA. Variations in atmospheric angular momentum on global and regional scales and the length of day. *Journal of Geophysical Research*. 1983;88(C9):5451–5470. Available from: <https://doi.org/10.1029/JC088iC09p05451>.
32. Iskenderian H, Salstein DA. Regional sources of mountain torque variability and high-frequency fluctuations in atmospheric angular momentum. *Monthly Weather Review*. 1998;126(6):1681–1694. Available from: [https://doi.org/10.1175/1520-0493\(1998\)126<1681:RSOMTV>2.0.CO;2](https://doi.org/10.1175/1520-0493(1998)126<1681:RSOMTV>2.0.CO;2).
33. Weickmann KM, Robinson WA, Penland C. Stochastic and oscillatory forcing of global atmospheric angular momentum. *Journal of Geophysical Research: Atmospheres*. 2000;105(12):15543–15557. Available from: <https://doi.org/10.1029/2000JD900198>.
34. Oort AH, Peixóto JP. Global angular momentum and energy balance requirements from observations. *Advances in Geophysics*. 1983;25(C):355–490. Available from: [https://doi.org/10.1016/S0065-2687\(08\)60177-6](https://doi.org/10.1016/S0065-2687(08)60177-6).
35. Huang HP, Weickmann KM. On the computation of the mountain torque from gridded global datasets. *Monthly Weather Review*. 2008;136(10):4005–4009. Available from: <https://doi.org/10.1175/2008MWR2359.1>.
36. Newton CW. Mountain torques in the global angular momentum balance. *Journal of the Atmospheric Sciences*. 1971;28(4):623–628. Available from: [https://doi.org/10.1175/1520-0469\(1971\)028<0623:mtiga>2.0.co;2](https://doi.org/10.1175/1520-0469(1971)028<0623:mtiga>2.0.co;2).
37. Kim Y-J, Eckermann SD, Chun H-Y. An overview of the past, present and future of gravity-wave drag parametrization for numerical climate and weather prediction models. *Atmosphere-Ocean*. 2003;41(1):65–98. Available from: <https://doi.org/10.3137/ao.410105>.
38. Berrisford P, Källberg P, Kobayashi S, et al. Atmospheric conservation properties in ERA-Interim. *Quarterly Journal of the Royal Meteorological Society*. 2011;137(659):1381–1399. Available from: <https://doi.org/10.1002/qj.864>.
39. Gong H, Huang M, Zhu L, Shao Y. Long-term variations of atmospheric angular momentum and torque. *Meteorology and Atmospheric Physics*. 2019;131(6):1697–1711. Available from: <https://doi.org/10.1007/s00703-019-00663-y>.
40. Huang HP, Sardeshmukh PD, Weickmann KM. The balance of global angular momentum in a long-term atmospheric data set. *Journal of Geophysical Research: Atmospheres*. 1999;104(2):2031–2040. Available from: <https://doi.org/10.1029/1998JD200068>.
41. Rosen RD, Salstein DA, Nehrhorn T. Predictions of zonal wind and angular momentum by the NMC medium-range forecast model during 1985–89. *Monthly Weather Review*. 1991;119(1):208–217. Available from: [https://doi.org/10.1175/1520-0493\(1991\)119<0208:POZWAA>2.0.CO;2](https://doi.org/10.1175/1520-0493(1991)119<0208:POZWAA>2.0.CO;2).
42. Veerman MA, van Heerwaarden CC. Trends in and closure of the atmospheric angular momentum budget in the 20th century in ERA-20C. *Quarterly Journal of the Royal Meteorological Society*. 2019;145(724):2990–3003. Available from: <https://doi.org/10.1002/qj.3600>.
43. Wahr JM, Oort AH. Friction- and mountain-torque estimates from global atmospheric data. *Journal of the Atmospheric Sciences*. 1984;41(2):190–204. Available from: [https://doi.org/10.1175/1520-0469\(1984\)041<0190:FAMTEF>2.0.CO;2](https://doi.org/10.1175/1520-0469(1984)041<0190:FAMTEF>2.0.CO;2).
44. Weickmann KM, Kiladis GN, Sardeshmukh PD. The dynamics of intraseasonal atmospheric angular momentum oscillations. *Journal of the Atmospheric Sciences*. 1997;54(11):1445–1461. Available from: [https://doi.org/10.1175/1520-0469\(1997\)054<1445:TDOIAA>2.0.CO;2](https://doi.org/10.1175/1520-0469(1997)054<1445:TDOIAA>2.0.CO;2).
45. Czarnetzki AC. Regional mountain torque estimates over the Rocky Mountains in lee cyclones. *Journal of the Atmospheric Sciences*. 1997;54(15):1986–1997. Available from: [https://doi.org/10.1175/1520-0469\(1997\)054<1986:RMTEOT>2.0.CO;2](https://doi.org/10.1175/1520-0469(1997)054<1986:RMTEOT>2.0.CO;2).
46. Wolf WL, Smith RB. Length-of-day changes and mountain torque during El Niño. *Journal of the Atmospheric Sciences*. 1987;44(24):3656–3660. Available from: [https://doi.org/10.1175/1520-0469\(1987\)044<3656:LODCAM>2.0.CO;2](https://doi.org/10.1175/1520-0469(1987)044<3656:LODCAM>2.0.CO;2).
47. Anderson JR, Rosen RD. The latitude-height structure of 40–50 day variations in atmospheric angular momentum. *Journal of the Atmospheric Sciences*. 1983;40(6):1584–1591. Available from: [https://doi.org/10.1175/1520-0469\(1983\)040<1584:TLHSOD>2.0.CO;2](https://doi.org/10.1175/1520-0469(1983)040<1584:TLHSOD>2.0.CO;2).
48. Dickey JO, Ghil M, Marcus SL. Extratropical aspects of the 40–50 day oscillation in length-of-day and atmospheric angular momentum. *Journal of Geophysical Research: Atmospheres*. 1991;96(D12):22643–22658. Available from: <https://doi.org/10.1029/91jd02339>.
49. Gensini VA, Allen JT. U.S. Hail frequency and the Global Wind Oscillation. *Geophysical Research Letters*. 2018;45(3):1611–1620. Available from: <https://doi.org/10.1002/2017GL076822>.
50. Gensini VA, Marinaro A. Tornado frequency in the United States related to global relative angular momentum. *Monthly Weather Review*. 2016;144(2):801–810. Available from: <https://doi.org/10.1175/MWR-D-15-0289.1>.
51. Weickmann K. Mountains, the global frictional torque, and the circulation over the Pacific-North American region. *Monthly Weather Review*. 2003;131(11):2608–2622. Available from: [https://doi.org/10.1175/1520-0493\(2003\)131<2608:MTGFTA>2.0.CO;2](https://doi.org/10.1175/1520-0493(2003)131<2608:MTGFTA>2.0.CO;2).
52. Weickmann K, Berry E. A synoptic-dynamic model of subseasonal atmospheric variability. *Monthly Weather Review*. 2007;135(2):449–474. Available from: <https://doi.org/10.1175/MWR3293.1>.
53. Wheeler MC, Hendon HH. An all-season real-time multivariate MJO index: development of an index for monitoring and prediction. *Monthly Weather Review*. 2004;132(8):1917–1932. Available from: [https://doi.org/10.1175/1520-0493\(2004\)132<1917:AARMMI>2.0.CO;2](https://doi.org/10.1175/1520-0493(2004)132<1917:AARMMI>2.0.CO;2).
54. Madden RA, Julian PR. Description of global-scale circulation cells in the tropics with a 40–50 day period. *Journal of the Atmospheric Sciences*. 1972;29(6):1109–1123. Available from: [https://doi.org/10.1175/1520-0469\(1972\)029<1109:dogscc>2.0.co;2](https://doi.org/10.1175/1520-0469(1972)029<1109:dogscc>2.0.co;2).

55. Kutzbach JE. Large-scale features of monthly mean Northern Hemisphere anomaly maps of sea-level pressure. *Monthly Weather Review*. 1970;98(9):708–716. Available from: [https://doi.org/10.1175/1520-0493\(1970\)098<708:lsfomm>2.3.co;2](https://doi.org/10.1175/1520-0493(1970)098<708:lsfomm>2.3.co;2).
56. Lambert SB, Marcus SL, De Viron O. Atmospheric torques and Earth's rotation: what drove the millisecond-level length-of-day response to the 2015–2016 El Niño? *Earth System Dynamics*. 2017;8(4):1009–1017. Available from: <https://doi.org/10.5194/esd-8-1009-2017>.
57. Dickey JO, Marcus SL, Hide R. Global propagation of interannual fluctuations in atmospheric angular momentum. *Nature*. 1992;357(6378):484–488. Available from: <https://doi.org/10.1038/357484a0>.
58. Lee RW, Woolnough SJ, Charlton-Perez AJ, Vitart F. ENSO modulation of MJO teleconnections to the North Atlantic and Europe. *Geophysical Research Letters*. 2019;46(22):13535–13545. Available from: <https://doi.org/10.1029/2019GL084683>.
59. Fernandes LG, Grimm AM. ENSO modulation of global MJO and its impacts on South America. *Journal of Climate*. 2023;36(22):7715–7738. Available from: <https://doi.org/10.1175/JCLI-D-22-0781.1>.
60. Baxter S, Weaver S, Gottschalck J, Xue Y. Pentad evolution of wintertime impacts of the Madden-Julian oscillation over the contiguous United States. *Journal of Climate*. 2014;27(19):7356–7367. Available from: <https://doi.org/10.1175/JCLI-D-14-00105.1>.
61. Weickmann K, Berry E, Gensini V, Gold D, Petroski T. Changes in the global climate: atmospheric angular momentum and Pacific Ocean temperatures. *Journal of Climate*. 2023;36(19):6597–6611. Available from: <https://doi.org/10.1175/JCLI-D-22-0322.1>.